J. Fluid Mech. (2007), *vol.* 576, *pp.* 425–444.
doi:10.1017/S0022112007004727 Printed in the United Kingdom

Effect of streamwise-periodic wall transpiration on turbulent friction drag

M. QUADRIO[1], J. M. FLORYAN[2] AND P. LUCHINI[3]

[1]Department of Aerospace Engineering, Politecnico di Milano, Italy

[2]Department of Mechanical and Materials Engineering, University of Western Ontario, Ontario, Canada

[3]Department of Mechanical Engineering, Università di Salerno, Italy

(Received 11 May 2004 and in revised form 29 October 2006)

In this paper a turbulent plane channel flow modified by a distributed transpiration at the wall, with zero net mass flux, is studied through direct numerical simulation (DNS) using the incompressible Navier–Stokes equations. The transpiration is steady, uniform in the spanwise direction, and varies sinusoidally along the streamwise coordinate. The transpiration wavelength is found to dramatically affect the turbulent flow, and in particular the frictional drag. Long wavelengths produce large drag increases even with relatively small transpiration intensities, thus providing an efficient means for improved turbulent mixing. Shorter wavelengths, on the other hand, yield an unexpected decrease of turbulent friction. These opposite effects are separated by a threshold of transpiration wavelength, shown to scale in viscous units, related to a longitudinal length scale typical of the near-wall turbulence cycle. Transpiration is shown to affect the flow via two distinct mechanisms: steady streaming and direct interaction with turbulence. They modify the turbulent friction in two opposite ways, with streaming being equivalent to an additional pressure gradient needed to drive the same flow rate (drag increase) and direct interaction causing reduced turbulent activity owing to the injection of fluctuationless fluid. The latter effect overwhelms the former at small wavelengths, and results in a (small) net drag reduction. The possibility of observing large-scale streamwise-oriented vortical structures as a consequence of a centrifugal instability mechanism is also discussed. Our results do not demonstrate the presence of such vortices, and the same conclusion can be arrived at through a stability analysis of the mean velocity profile, even though it is possible that a higher value of the Reynolds number is needed to observe the vortices.

1. Introduction

One of the most effective means of modifying a turbulent wall-bounded flow is the use of suction or blowing at the wall. Suction is often used as an aerodynamic flow-control technique to prevent laminar–turbulent transition and flow separation (Gad-el Hak & Bushnell 1991), whereas blowing can provide insulation between a hot gas and the solid wall (Ahn, Sung Jung & Lee 2003). A detailed knowledge of the effects of *spatially uniform, steady* transpiration on the turbulent flow in a plane channel or boundary layer is currently available, thanks to a number of experiments and numerical simulations. Sumitani & Kasagi (1995) for example investigated with a direct numerical simulation (DNS) the turbulent flow in a channel, where uniform suction was applied at one wall and uniform injection at the opposite wall. They detailed how the turbulent friction, the heat transfer and other turbulence statistics

depend on the intensity of the wall forcing, and confirmed that suction increases friction and decreases turbulent fluctuations, while blowing has the opposite effect.

Other studies focused on the spatial response of the turbulent flow to a *spatially localized, steady* suction or blowing. For example Antonia, Zhu & Sokolov (1995) experimentally investigated the effect of suction or blowing through a small spanwise slot in the wall on a turbulent boundary layer, describing changes in the flow properties as the flow recovers its original state downstream of the slot. Park & Choi (1999) made a similar DNS-based investigation by considering a lower forcing intensity compared to previous investigations. All these studies describe the steady transpiration in terms of a single parameter, namely the flow rate given by the product of the transpiration velocity and the gap width.

Spatially distributed, unsteady forcing of a turbulent channel flow was employed by Choi, Moin & Kim (1994) in a numerical simulation of an active control strategy (the so-called 'opposition control'). They imposed as time-dependent boundary condition at each point of the wall a transpiration velocity equal and opposite to the local wall-normal component at $y^+ = 10$, and obtained a reduction of the friction drag of more than 20 %, so demonstrating that in principle a suitable arrangement of zero-net-mass-flux transpiration can lead to significant reduction of friction. Another approach is that of Park, Lee & Sung (2001), who applied a *spatially localized, unsteady* sinusoidal-in-time wall-normal velocity at a narrow spanwise slot in a turbulent boundary layer DNS. A related experimental study was presented by Tardu (2001), who considered localized time-dependent blowing, with a velocity oscillating sinusoidally in time from zero to its maximum value, i.e. a blowing with non-zero net mass flux. In both cases the unsteady flow from the slot or the orifice was found to affect turbulence in a complex way as the flow evolves downstream of the slot. The effect of the forcing was moreover shown to depend upon its temporal frequency.

In this work we shall study through DNS the effects of a *spatially distributed, steady* low-amplitude transpiration. We shall focus on the transpiration represented by a single sinusoidal wave, characterized by its amplitude A and its longitudinal wavenumber α_t (or, equivalently, its wavelength $\lambda_t = 2\pi/\alpha_t$). We are interested in low-amplitude transpiration primarily due to the cost associated with its creation in real systems, and our main objective is to investigate whether and how the turbulent flow is modified by the selection of a properly distributed transpiration.

To our knowledge, the only paper dealing, though only partially, with the same flow configuration is that by Jiménez *et al.* (2001). They investigated numerically the effect of a wall transpiration proportional to the local instantaneous value of pressure fluctuations, i.e. they modelled a passive porous surface, and found that the skin friction increases by up to 40 % without flow separation. The increase is reportedly due to a large-scale reorganization of the flow: the transpiration adjusts itself into a two-dimensional spanwise-coherent pattern, producing large rolls of spanwise vorticity, with a preferred streamwise wavelength of approximately 500 viscous lengths. Jiménez *et al.* (2001) in a subset of their numerical experiments studied so-called active porous walls, i.e. exactly the same flow that is the subject of the present paper. Ten flow conditions were considered, by varying the strength of the imposed transpiration and its phase velocity, but the wavelength was kept fixed at the value suggested by the naturally occurring rolls in the passive porosity case. With active transpiration they again found friction increases up to 40 %. Jiménez *et al.* (2001) also performed a linear stability analysis, by using the mean turbulent velocity profile as the base flow and a variable turbulent eddy viscosity, with the aim of checking whether the two-dimensional pattern was caused by an instability mechanism. They found that this is

indeed the case: at the porosity levels considered, spanwise-coherent fluctuations with wavelengths longer than approximately 350 viscous lengths turn out to be unstable, growing into the observed spanwise vorticity rolls. The aim of the present paper is to complete the assessment of the effects of the sinusoidal transpiration on the turbulent flow, by investigating in greater detail how they are function of the two parameters A and λ_t. Moving transpiration patterns (phase velocity different from zero), as well as patterns generated by the superposition of multiple Fourier modes will not be considered.

The present work was also motivated by a second question, for which we have not obtained a definite answer: whether sinusoidal transpiration is able to generate large-scale vortical structures oriented in the streamwise direction, as a consequence of a centrifugal instability mechanism, in analogy with the laminar case (Floryan 1997). We shall briefly discuss this issue in § 5, in connection with the results of stability calculations that start from the turbulent mean velocity profile and follow the procedure described by Floryan (1997) for a laminar flow, arguing (Crighton & Gaster 1976) that turbulence sets up an equivalent laminar flow profile for large-scale coherent motions.

The structure of the paper is as follows. In § 2 the numerical method and the computer code employed for the numerical simulations are briefly described, and § 2.1 illustrates the spatio-temporal discretization and the parameters adopted in the simulations. (The Appendix deals with accuracy and error estimation.) In § 3 we report results concerning the modification of the mean friction through sinusoidal transpiration at different wavelengths and intensities, with focus on the drag-reducing regime. A discussion of the physical mechanisms responsible for the change in friction drag is presented in § 4, and § 5 addresses the issue of large-scale vortices, while § 6 is devoted to the conclusions.

2. The numerical method

Our DNS code is a parallel solver of the Navier–Stokes equations for an incompressible fluid. A description of the numerical method can be found in Luchini & Quadrio (2006). It is based on a mixed discretization: a Fourier expansion is used for the wall-parallel directions, and high-accuracy compact (explicit) finite-differences schemes are used in the wall-normal direction, to obtain an efficient parallel implementation with low communication requirements. Aside from the advantages of parallel computing discussed by Luchini & Quadrio (2006), when a non-zero vertical velocity is applied at the wall the use of finite differences in the wall-normal direction reduces the time-step restriction that would be present if a Chebyshev discretization were used (Jiménez *et al.* 2001).

The Navier–Stokes equations are formulated, following Kim, Moin & Moser (1987), in terms of two scalar equations for the normal component of velocity and the normal component of vorticity, thus achieving the highest computational efficiency when a Fourier discretization is adopted for the homogeneous directions. The nonlinear terms of the equations are computed by a pseudo-spectral approach, using efficient fast-Fourier-transforms algorithms and dealiasing in the homogeneous directions. The time advancement employs the widespread partially implicit approach: nonlinear terms are advanced with an explicit method (a low-storage three-substeps third-order Runge–Kutta scheme), and linear terms are advanced with an implicit method (a second-order Crank–Nicolson scheme) to overcome the stability limitations due to the viscous terms.

2.1. *Computational parameters*

The simulations described in the following have been carried out at a value of the Reynolds number $Re = U_b h/\nu$ of 2833, based on the bulk mean velocity U_b and the channel half-width h. This corresponds to a Reynolds number based on the friction velocity of $Re_\tau = 180$ and to $Re_c = 3300$ when the centreline velocity U_c is used as reference velocity. A few cases at $Re = 7000$ or $Re_\tau = 400$ will also be discussed. As an alternative to scaling with h and U_b, viscous scaling will also be used in the following: quantities indicated with a $+$ superscript are made non-dimensional by using the fluid viscosity and the friction velocity of the reference flow.

We use a coordinate system where x, y and z denote the streamwise, wall-normal and spanwise directions respectively. The corresponding velocity components are taken as u, v and w. The boundary conditions in the streamwise and spanwise directions are periodic, and the transpiration is accounted for through the wall boundary condition for the wall-normal velocity component:

$$v(x, \pm 1, z) = A \cos(\alpha_t x), \tag{2.1}$$

where A is the maximum amplitude of the transpiration. The wavenumber α_t is chosen to be an integer multiple of the fundamental wavenumber in the streamwise direction, $\alpha_0 = 2\pi/L_x$, so that the transpiration has a zero net mass flux over each wall.

In the simulations the streamwise flow rate Q_x is kept fixed, and a zero mean spanwise pressure gradient is imposed. The length and width of the computational domain, as well as the spatial resolution at $Re_\tau = 180$, have been chosen following Kim *et al.* (1987): we will use $L_x = 4\pi h$ and $L_z = 2\pi h$, with $N_x = 192$, $N_y = 129$ and $N_z = 160$. In a few cases the number of points for each spatial direction is doubled, to account for the increased resolution requirements due to high-amplitude transpiration. The cases at $Re_\tau = 400$ have a correspondingly increased number of modes, for a total of more than 6×10^7 degrees of freedom. The Appendix addresses the estimated accuracy of the computed statistics, in particular of the friction coefficient.

Each simulation is started from a fully developed turbulent flow field computed in a previous simulation (for the given Re and spatial resolution) with transpiration turned off, and is run for a total integration time of approximately 4000 and 7500 viscous time units for the low- and high-Re cases respectively. The time evolution of selected quantities, notably the two components of the space-averaged friction over the walls, is recorded. When transpiration is turned on, there is an initial transient where the flow adapts to its new quasi-equilibrium state. This transient is evident in the time history of the space-averaged friction, and is discarded from the calculation of the time-averaged value of C_f. Turbulence statistics are computed from flow fields stored on disk during the calculation: we average over at least 30 fields separated from each other by $\approx$120 viscous time units, written to disk after discarding the initial transient. In addition, friction data from the two walls are averaged to increase the statistical sample.

3. The mean friction

We have carried out one reference simulation without transpiration, and many cases with different combinations of A and α_t, to measure the time-averaged value of the space-mean friction coefficient:

$$C_f = \frac{2\tau_x}{\rho U_b^2}, \tag{3.1}$$

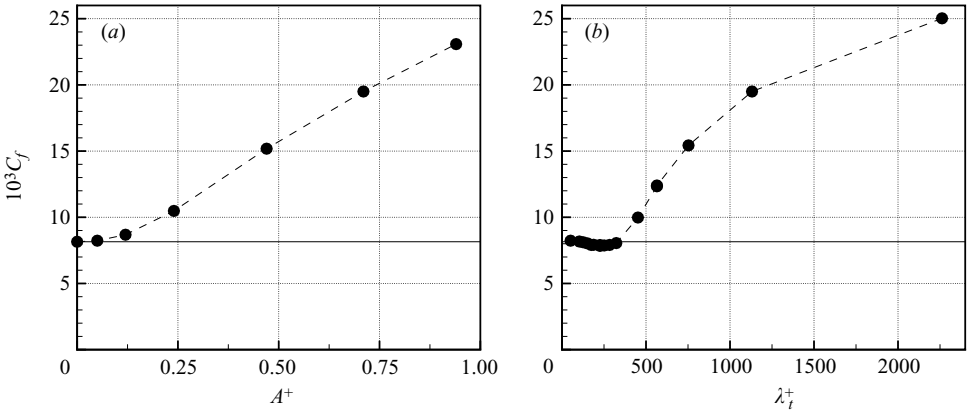

FIGURE 1. Friction coefficient versus (*a*) transpiration intensity A^+ at fixed wavelength $\lambda_t^+ = 1130$, and (*b*) wavelength λ_t^+ at fixed amplitude $A^+ = 0.7$. The horizontal line marks the value of C_f in the impermeable case.

where τ_x is the longitudinal component of the shear stress at the wall, and ρ is the fluid density.

Figure 1(*a*) plots the friction coefficient as a function of the transpiration intensity A^+, with the wavenumber fixed at $\alpha_t = 2\alpha_0$ corresponding to a forcing wavelength of $\lambda_t^+ = 1130$. The friction coefficient is observed to increase linearly with A^+, and even with modest intensities the increase in C_f is three-fold. A threshold of minimum A^+ is required for the transpiration to affect the turbulent flow: the minimum intensity at this wavelength is $A^+ \approx 0.05$, below which the change in C_f becomes comparable with the measurement uncertainty (see the Appendix).

Figure 1(*b*) shows how C_f changes with the transpiration wavelength, for fixed amplitude $A^+ = 0.7$. This plot shows that, as long as $\lambda_t^+ > 350$, there is a significant increase in friction which tends to reach a plateau at large values of λ_t^+.

The region in figure 1(*b*) at small values of λ_t^+ deserves particular attention. The same data are reported with filled circles in figure 2, which enlarges this region. For wavelengths $100 < \lambda_t^+ < 350$, the friction coefficient goes below the reference value, i.e. the turbulent flow experiences a decrease of the frictional drag. The maximum drag reduction with $A^+ = 0.7$ is 3.7 % at $\lambda_t^+ = 226$. This percentage change in C_f, though rather small, is shown by resolution studies (presented in the Appendix) to be larger than the uncertainty associated with the discretization. The Appendix also illustrates different checks, such as the use of transpiration over the two walls shifted by half a wavelength each, and the use of transpiration over a single wall. The negligible dependence of ΔC_f on these parameters indicates that the accuracy of the present results is sufficient to claim a decrease in frictional drag.

The open symbols in figure 2 are for a few cases run at $Re_\tau = 400$ and with correspondingly increased spatial resolution. They are very important, since they confirm that the drag reduction phenomenon is not a low-*Re* artifact. Moreover, the results of two sets of simulations carried out at significantly different values of *Re* highlight the wall-units scaling of the governing parameters for drag reduction, which is obtained via a wall-based forcing.

When λ_t^+ is in the optimum range, C_f decreases as the intensity of the transpiration is increased: figure 3 reports the entire range $0 < A^+ < 4.7$. Open circles correspond

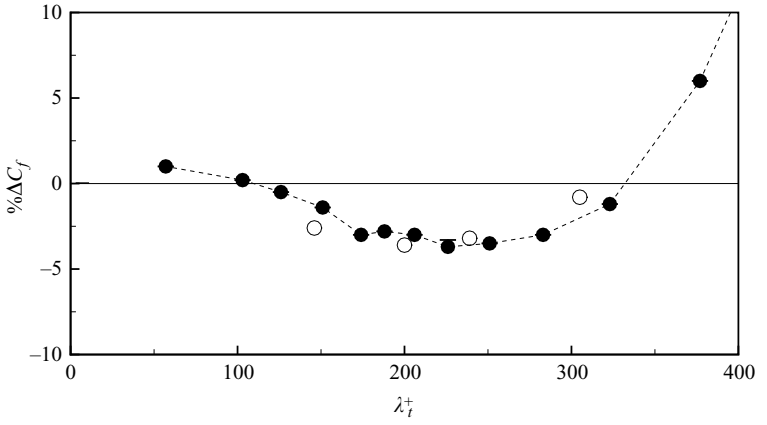

FIGURE 2. Percentage variation of the friction coefficient $\%\Delta C_f = 100(C_{f,t} - C_{f,0})/C_{f,0}$ versus transpiration wavelength λ_t^+, at fixed intensity $A^+ = 0.7$. Filled circles, $Re_\tau = 180$; open circles, $Re_\tau = 400$. The error bar for the point at $\lambda_t^+ = 225$ indicates the error estimate reported in the Appendix (table 1).

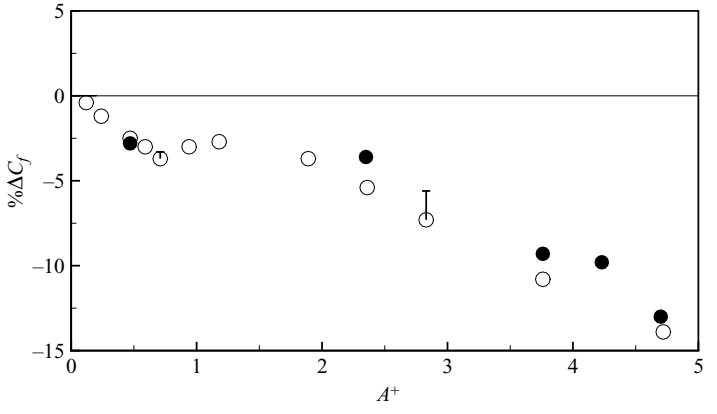

FIGURE 3. Percentage variation of the friction coefficient $\%\Delta C_f = 100(C_{f,t} - C_{f,0})/C_{f,0}$ versus intensity A^+, at fixed $\lambda_t^+ = 226$ and $Re_\tau = 180$. Open circles are cases with baseline resolution; error bars refer to error estimates reported in the Appendix (table 1). Filled circles have the spatial resolution doubled in each coordinate direction, and are thus quantitatively more reliable.

to simulations at $Re_\tau = 180$ and baseline resolution, and show clearly a trend of increasing drag reduction with increasing A^+. The resolution study described in the Appendix indicates, however, that beyond some amplitude threshold the baseline resolution is no longer sufficient to guarantee truly resolution-independent results: this can be appreciated from the two error bars, since the one at $A^+ = 2.8$ is not negligible in comparison to $\%\Delta C_f$. Selected simulations have thus been repeated with spatial resolution doubled for each spatial direction (and the time-step size reduced accordingly). The increase of drag reduction with A^+ is fully confirmed by these highly resolved simulations, and we have reached a value of 13 % for the highest tested value of $A^+ = 4.7$.

4. Discussion

Wall transpiration alters the friction coefficient of the turbulent flow, through one (or both) of two distinct mechanisms: (i) direct interaction with the turbulence, and (ii) streaming induced by the transpiration wave. Our first aim is to discriminate between these two physical processes, and to ascertain their relative importance.

Streaming (or steady streaming or acoustic streaming) is the phenomenon, already known to Rayleigh (1883), by which an oscillatory flow may result in a non-zero mean. Several flows where steady streaming is important have been discussed in the review article by Riley (2001). Streaming takes place whenever a wave in relative motion with respect to a fluid undergoes viscous dissipation; we may have streaming in the present flow because the transpiration wave is fixed in space while the flow convects downstream. The important effect of streaming is an additional flow rate (or thrust) that adds to any drag change due to turbulence modification: streaming creates a flow rate – in a direction to be determined – without a pressure gradient.

To establish the relative importance of mechanisms (i) and (ii), we consider the streamwise component of the mean momentum equation. Instead of the usual average over time and homogeneous directions, however, the dependence of flow statistics on the streamwise coordinate is retained. When statistics are averaged over x too, the usual full average is obtained, indicated with $\langle\cdot\rangle$. We shall indicate with a tilde quantities averaged over t and z only, e.g. $\widetilde{u}=\widetilde{u}(x, y)$. It follows by definition that

$$\langle u(y)\rangle = \frac{1}{L_x}\int_0^{L_x} \widetilde{u}(x', y)\,\mathrm{d}x'.$$

The tilde-averaged x component of the momentum equation becomes

$$0 = \frac{1}{Re}\frac{\mathrm{d}^2\widetilde{u}}{\mathrm{d}y^2} - \frac{1}{\rho}\frac{\mathrm{d}p}{\mathrm{d}x} - \frac{\mathrm{d}}{\mathrm{d}y}[\widetilde{(u-\widetilde{u})(v-\widetilde{v})} + \widetilde{u}\widetilde{v}].$$

The last term is absent in the impermeable case, where $\widetilde{v}\equiv 0$, so that it becomes natural to associate it with streaming, whereas the difference in $\widetilde{(u-\widetilde{u})(v-\widetilde{v})}$ between the impermeable and porous case is taken as an indicator of the direct interaction of transpiration with turbulence. Two representative simulations with transpiration are considered at $Re_\tau = 180$, with the same discretization parameters as described in § 2.1. The main difference between these cases and those described in § 3 is that they are under the constraint of constant pressure gradient, instead of constant flow rate. The first case has $A^+ = 0.9$ and $\lambda_t^+ = 565$, and results in a drag increase; the second case with $A^+ = 0.57$ and $\lambda_t^+ = 226$ presents a decreased drag.

Figure 4 reports the profile of the quantity $Re_\tau \int_0^y (\widetilde{u}\widetilde{v})^+ \mathrm{d}y'$, together with the difference between the reference mean velocity profile and the profile with transpiration. The integral in y of this latter quantity expresses the increase or decrease of flow rate due to transpiration as a whole; the integral of the former is the contribution by streaming alone. It follows that the difference between the two can be associated with the direct effect of transpiration on turbulence.

For the drag-increasing case, the global effect is a decrease of the flow rate by $-10.8\,\%$ compared to the impermeable case. The contribution by streaming alone is an even larger decrease (namely $-13.1\,\%$). Hence the direct interaction with turbulence, though smaller, is in the opposite direction and increases the flow rate by $+2.3\,\%$. The drag-decreasing case presents a consistent behaviour. Here the flow rate increases by $+1.5\,\%$, consistently with the reduced friction. The contribution due to streaming is still negative ($-2.0\,\%$), and is counterbalanced by the remaining $+3.5\,\%$.

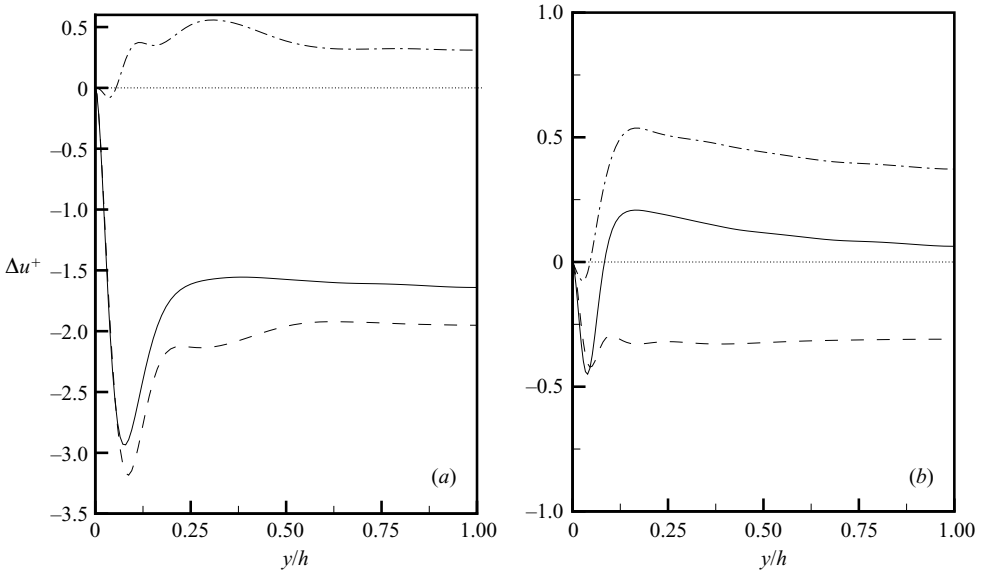

FIGURE 4. Changes in the mean velocity profile for (*a*) a drag-increasing and (*b*) a drag-reducing case. Continuous line: total change in the mean velocity profile; dashed line: contribution by streaming alone; dash-dotted line: contribution associated with the effect of transpiration. Velocities are expressed in wall units. Note the different scale on the ordinate in the two plots.

4.1. *Flow statistics*

To understand the drag reduction phenomenon, we focus on the changes induced by wall transpiration on the near-wall turbulence, with the aid of turbulence statistics. Two cases will be considered, with the same $A^+ = 0.57$ and a long and a short wavelength: the first (case L) has $\lambda_t^+ = 565$ and an increased frictional drag, whereas the second (case S) has $\lambda_t^+ = 226$ and decreased drag. These simulations have been run at a constant value of the flow rate.

We first consider, in figure 5, the streamwise evolution of the local friction coefficient $\widetilde{C}_f(x)$ along the transpiration wave, normalized to unit mean value. The effect of transpiration is larger for the longer wavelength, thus confirming the role of the flow rate Q_t through the transpiration half-wave, but the qualitative behaviour is similar. The local friction is always positive (there is no backflow), and remains below its average value in regions where the transpiration velocity is positive (blowing). It remains below the average even in a non-negligible portion of the region where the transpiration velocity is negative (suction). This effect is more pronounced for case S. Owing to suction, $\widetilde{C}_f$ eventually rises above the mean, but its local maximum occurs appreciably downstream of the location of maximum suction. Shortly thereafter, and still during the suction phase, $\widetilde{C}_f$ decreases again, and eventually, through the action of blowing, drops below its mean value. The flow response to the wall blowing is thus more local, without the phase lag that is observed between suction and drag increase. This is in line with the observations by Chung, Sung & Krogstad (2002), who reported, for the response of a wall flow suddenly subjected to uniform transpiration of either sign, a spatial delay which is larger for suction than for blowing. The drag reduction effect could be rooted in the difference between the transpiration wavelength and this spatial delay.

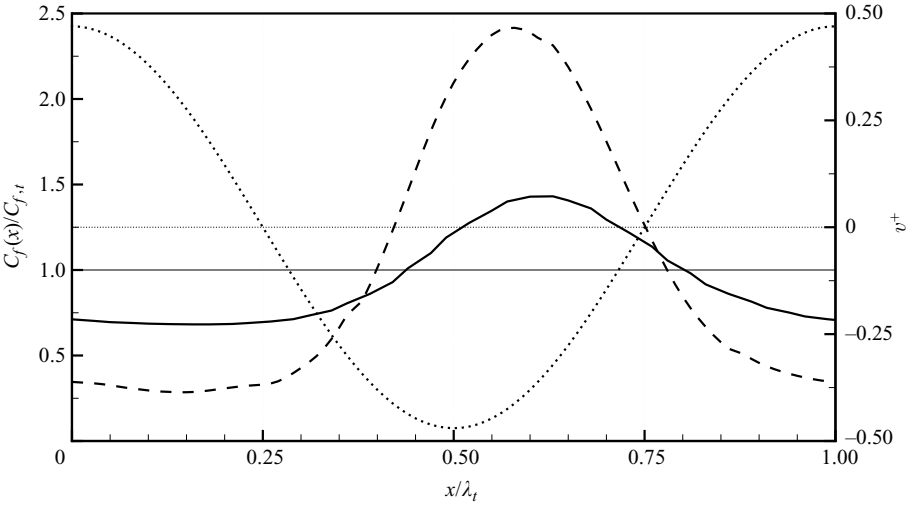

FIGURE 5. Local friction coefficient $\widetilde{C}_f(x)$ along the transpiration wave, normalized with its mean value $C_{f,t}$, for $\lambda_t^+ = 226$ (case *S*, continuous curve) and $\lambda_t^+ = 565$ (case *L*, dashed curve), both with the same intensity $A^+ = 0.47$. The dotted curve represents the sinusoidal behaviour of the transpiration velocity along the wall, with maxima and minima of $\pm A^+$ (right-hand axis).

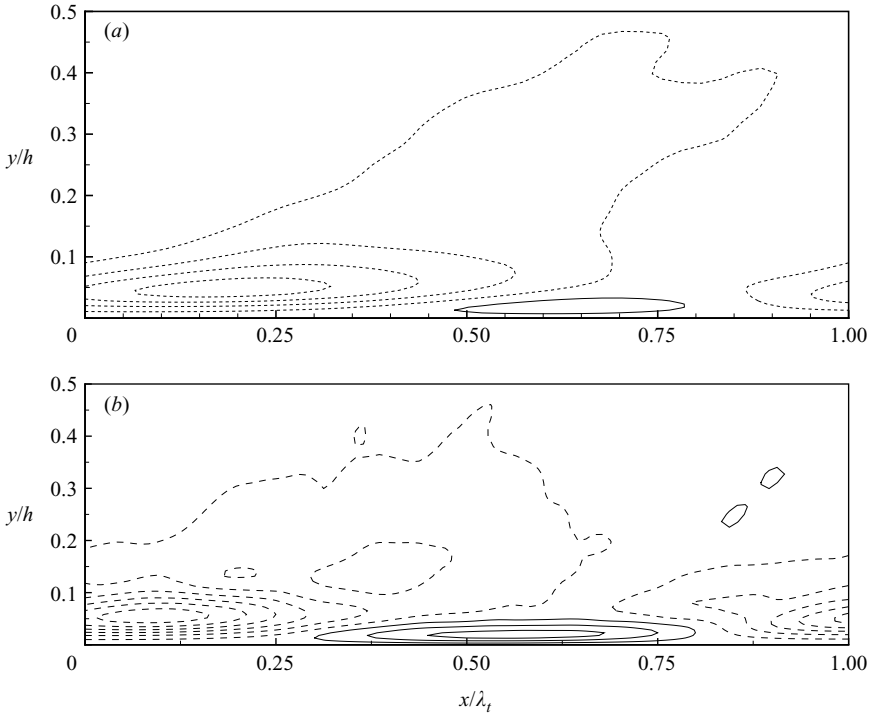

FIGURE 6. Variation $\Delta\mathscr{K}^+$ of local turbulent kinetic energy with respect to the impermeable case: (*a*) case *S* and (*b*) case *L*. Contour spacing 0.2, dashed lines represent negative levels.

We consider now in figure 6 the turbulent kinetic energy $\mathscr{K}$, calculated from the velocity fluctuations around the local mean, and defined as follows:

$$\mathscr{K}(x, y) = \frac{1}{2}((u - \widetilde{u})^2 + (v - \widetilde{v})^2 + (w - \widetilde{w})^2).$$

Figure 6 reports the spatial distribution of the difference $\Delta\mathscr{K}^+$ between $\mathscr{K}^+$ over the transpirating wall and $\mathscr{K}^+ = \langle\mathscr{K}\rangle^+$ over the impermeable wall. The largest differences are located near the wall, and it can be seen that the wavelength does not affect the penetration depth at which the variations of $\mathscr{K}^+$ appear. $\mathscr{K}^+$ is reduced in the blowing region, and increased in the suction region, where fluctuationless fluid is injected into the flow, and increases in the suction region. In case L however, the positive and negative variations are roughly in balance, both in intensity and spatial extent, whereas in case S the decrease overwhelms the increase, thus yielding a global reduction.

The reduction of turbulent fluctuations is the basis of the drag-reducing mechanism. It has been shown quantitatively by Iwamoto *et al.* (2005) that the absence of near-wall fluctuations inhibits the momentum transfer by turbulence, and results in alleviated frictional drag. Through a DNS, where they could artificially annihilate turbulence fluctuations in a near-wall layer of arbitrary depth to simulate the effects of an hypothetical active control system, Iwamoto *et al.* (2005) have shown that drag decreases with increasing thickness of the fluctuationless layer. In our case, the thickness of the layer with reduced fluctuations increases with A^+: this explains the drag reduction behaviour reported in figure 3.

In figure 2 we see an inversion of the flow response to the transpiration at $\lambda_t^+ \approx 350$. Evidence has accumulated in recent years that this is indeed a typical longitudinal length scale in near-wall turbulence. Jiménez & Moin (1991) with their minimum channel DNS estimated at $L_x^+ \approx 300 - 400$ the minimal extent of the computational domain that is needed to sustain the turbulence cycle. This is also the typical length of the quasi-streamwise vortical structures described by Jeong *et al.* (1997). Their results, based on a specifically chosen indicator for the presence of vortices, indicate clearly that near the wall the dominant coherent structures are quasi-streamwise vortices with partial overlap in the streamwise direction. The basic flow unit, consisting of a pair of such vortices with opposite sense of rotation, has a streamwise extent of approximately 400 wall units. These results have been confirmed by Schoppa & Hussain (2002), who addressed the issue of the dynamical evolution of the coherent structures, and introduced the notion of streak transient growth to explain the generation of new streamwise vortices. Interestingly, they found that the streaks exhibit the strongest instability to spanwise velocity perturbations with a streamwise wavelength of 400 wall units. Moreover, the transient nonlinear energy growth reaches its maximum after 20–40 viscous time units, a time scale which compares well with the threshold value of λ_t^+ when converted into a spatial scale through a suitable value (Quadrio & Luchini 2003) of the near-wall convection velocity. Finally, the stability analysis carried out by Jiménez *et al.* (2001) has shown that, in the turbulent flow over passive porous walls (at Reynolds numbers and porosity levels comparable with the present ones), the roll-like dominant structures change their stability properties and become stable when their wavelength decreases below approximately 350 viscous lengths. This again suggests that the drag-increasing phenomena related to the sinusoidal forcing at the wall could work efficiently as long as the wavelength of the forcing is larger than this threshold.

The injection of fluctuationless fluid is visualized qualitatively in figure 7, which shows a case where the effects of the drag-reducing mechanism are made more evident by employing the larger value of $A^+ = 2.4$. An instantaneous representative flow field is considered, and contours of streamwise vorticity in an (x, y)-plane are shown. (Jeong *et al.* (1997) have demonstrated that in the near-wall region ω_x is a good qualitative indicator for streamwise vortices.) Each vortex appears to interact with

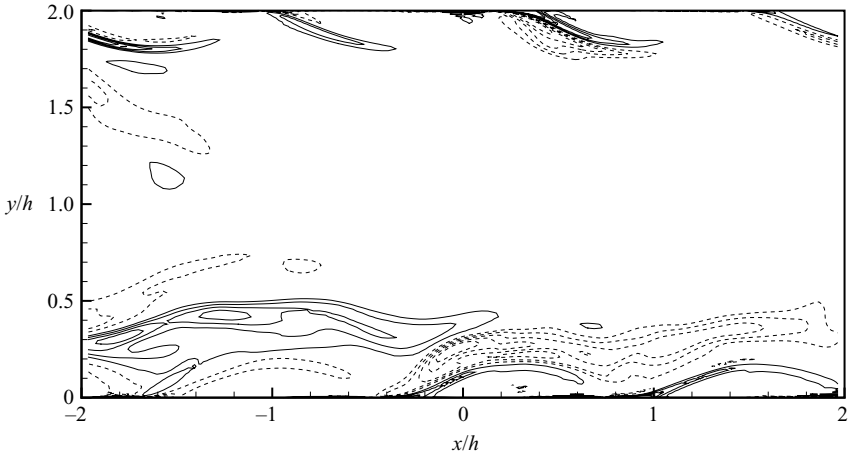

FIGURE 7. Two-dimensional spatial distribution of streamwise vorticity ω_x^+, in an x, y section of a representative flow field computed for $A^+ = 2.4$ and $\lambda_t^+ = 226$. Contours from -0.5 to 0.5 excluding 0, with 0.1 increments; negative values are dashed. Only a portion of the full streamwise length is shown.

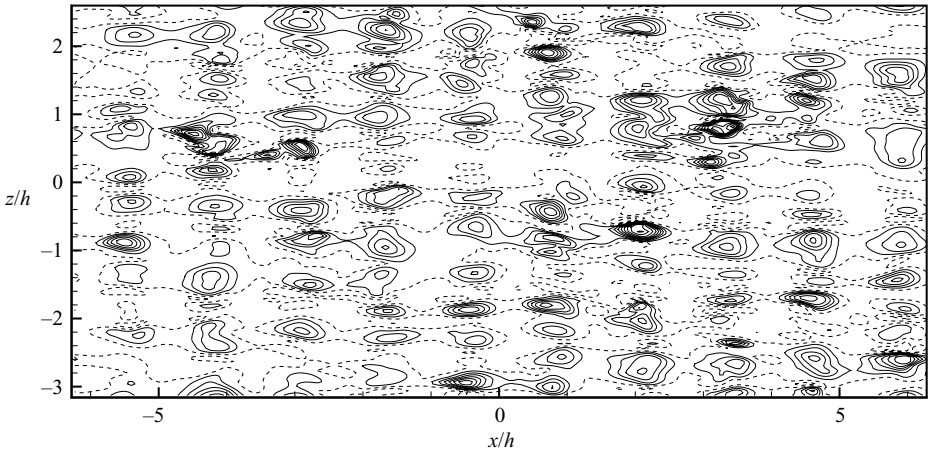

FIGURE 8. Two-dimensional, instantaneous spatial distribution of $u^+ - \langle u^+ \rangle$ at $y^+ \approx 5$ for case *S*. Contours are from -3 to 8.5 with unit increment, negative values are dashed.

the region of fluctuationless fluid injected into the channel from the wall through a strong layer of opposite-sign vorticity, much like the secondary vorticity which develops between the same vortex and an impermeable wall due to the kinematic consequences of the no-slip condition. This strong layer contributes to the weakening of the parent structure, which first becomes more inclined to the wall (see for example the top wall in figure 7), and eventually is ejected into the bulk of the flow (bottom wall).

The structure of near-wall turbulence is not affected dramatically by small-wavelength transpiration. In figure 8 the instantaneous field $u - \langle u \rangle$ at $y^+ \approx 5$ and case *S* is presented. The elongated low-speed regions are still present, though modulated by the transpiration wave. Note that the picture does not change qualitatively when the fluctuations around the local mean $\tilde{u}$ field are plotted instead. An effect of the suction

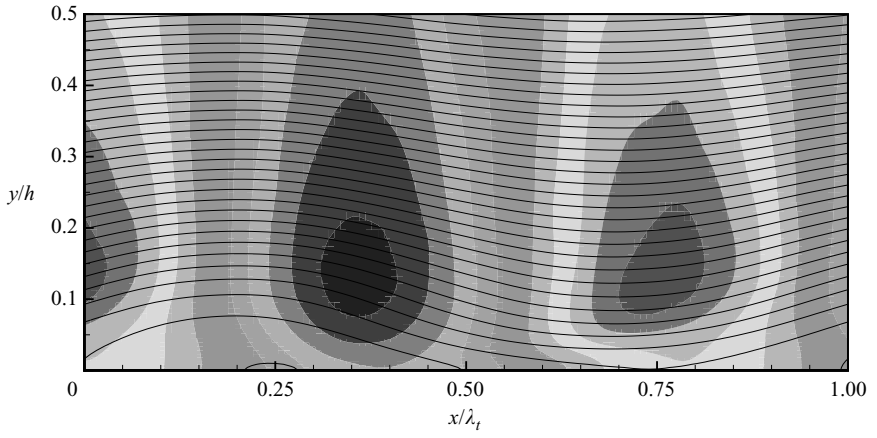

FIGURE 9. Mean streamlines for case L, over one full wavelength. The underlying colour levels indicate the mean wall-normal velocity field $\widetilde{v}^{+}(x, y)$, and are from -1 to 1 with increment 0.2.

is to create high-speed patches, aligned along the span, over the suction area. It is noteworthy that the longitudinal streaky structure of the flow completely disappears in case L (not shown), thus confirming that in this case the turbulence production mechanism near the wall is qualitatively altered by the transpiration.

5. Presence of large-scale streamwise vortices

One point of interest of the present flow is the possible presence of large-scale streamwise vortices, where the term 'large' refers to vortices extending throughout the whole channel gap. Such vortices might be of practical importance: they may lead to a significant drag reduction, as shown by Schoppa & Hussain (1998), or to an increase in turbulent mixing, as shown by Gschwind, Regele & Kottke (1995). According to Floryan (1997), such large-scale vortices may be created in a two-dimensional laminar Poiseuille flow by application of sinusoidal wall transpiration with zero net mass flux. Floryan (2003) describes in detail the generation of large-scale streamwise vortices in a laminar Couette flow with sinusoidal transpiration at the walls. Recent experiments show the appearance of large vortical structures in both laminar and turbulent flow in a channel with one wavy wall (Günther & Rudolph von Rohr 2003), though their visualization of a vortical structure in turbulent regime is a very difficult task. Similar vortices have been reportedly found in the turbulent boundary layer over a wavy wall (Gong, Taylor & Dörnbrack 1996), and in the interaction between a steady wind shear and surface waves in the ocean, where they are known as Langmuir circulations (Leibovich 1983).

The problem can be attacked by following two approaches. The obvious way is to search the DNS database for the presence of such vortices. An alternative strategy is to resort to the same tools, drawn from stability theory, which have demonstrated presence of vortices in the laminar regime. In this Section the outcomes and limitations of both approaches will be discussed.

5.1. *DNS analysis*

The vortices we are looking for would be generated by a centrifugal instability mechanism induced by curvature. DNS results show clearly that a significant curvature of the mean streamlines is indeed present. Streamlines are plotted in figure 9, together

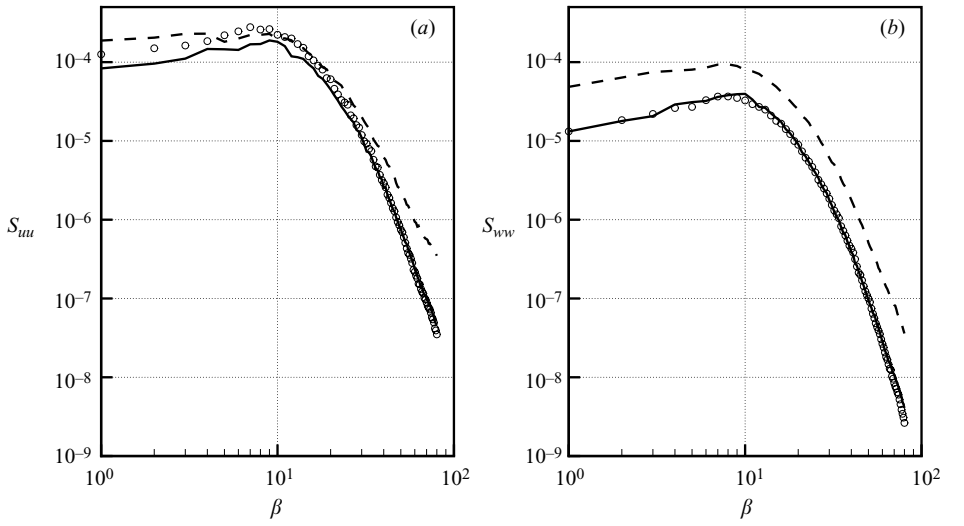

FIGURE 10. One-dimensional spanwise autospectral density function for (*a*) u and (*b*) w, evaluated at $y^+ \approx 5$: comparison between case L (dashed line), case S (continuous line), and the reference flow (symbols).

with the full $\widetilde{v}(x, y)$ field. The streamlines for case S (with small Q_t) show appreciable curvature up to $y/h \approx 0.1$, while in case L (with larger Q_t) their curvature extends through a significant portion of the channel.

If large-scale vortices, due to curvature effects, were present in the flow, they would show in one-dimensional autospectral density functions, like the one reported in figure 10, through a discernible peak at the preferred spanwise vortex wavenumber. These spectra are modified for the flow over the impermeable wall, but no evident peak can be observed. Various distances from the wall have been considered, and the same qualitative conclusion has been reached.

Figure 11 shows, comparing case S and case L, the streamwise evolution of the one-dimensional spanwise autocorrelation function $R_{uu}(\Delta z)$ for the longitudinal velocity component at $y^+ \approx 5$. The presence of vortices would translate into a constant region of negative correlation for some spanwise separation. It might be useful to recall that this is not a two-dimensional correlation, since the abscissa on the plot is the actual streamwise coordinate, while the other coordinate is the spanwise separation Δz. In the reference flow, this quantity does not present any x evolution. Again no evidence of streamwise vortices (neither at this y position nor at the others checked) can be found. In case S $R_{uu}(\Delta z)$ does not appreciably evolve over x/λ_t and is quantitatively similar to the impermeable case, whereas in case L transpiration has a direct effect on the turbulence structure near the wall, as already observed. The structure of $R_{uu}(\Delta z)$ is destroyed over the suction area, to partially recover over blowing.

5.2. *Stability theory*

Modelling large-scale coherent structures as instability 'modes' of the turbulent mean velocity profile is a questionable approach, which nevertheless has led to some success in the past. For example Crighton & Gaster (1976) considered a turbulent jet and argued that turbulence sets up an equivalent laminar flow profile for large-scale coherent modes, and arrived at numerical results which were supported by available measurements.

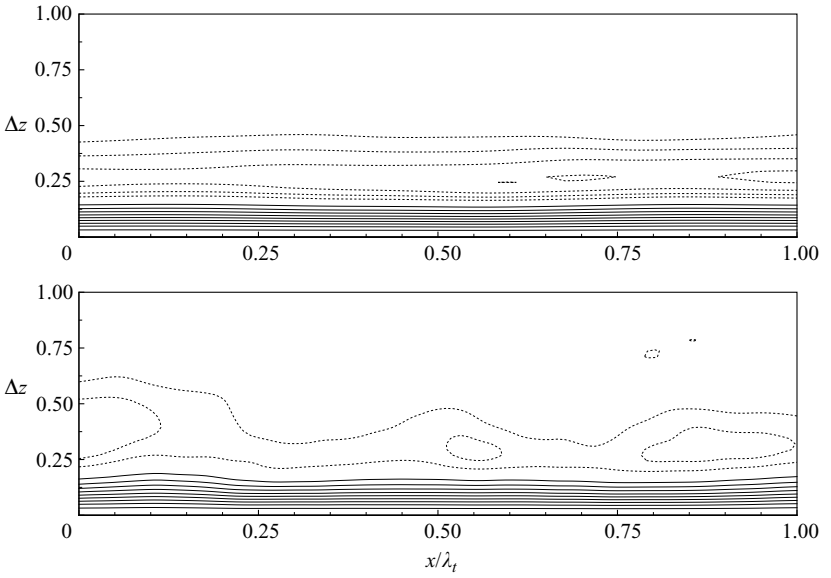

FIGURE 11. One-dimensional spanwise autocorrelation function $R_{uu}(\Delta z)$ along the transpiration wave, at $y^+ \approx 5$. Comparison between (*a*) case *S* and (*b*) case *L*. Contours are levels of the correlation coefficient from 0.1 with 0.1 increments. Negative values are dashed, from −0.05 with 0.05 decrements.

We have thus carried out such an analysis to further investigate the presence of large-scale vortices. The analysis consists of two main steps, and we refer the interested reader to Floryan (1997) for full details of the analysis and its numerical implementation in the laminar case. We start from the DNS-computed turbulent mean velocity profile over the impermeable wall, then the two-dimensional base flow induced by the transpiration is determined, and eventually the stability of this x-dependent base flow is studied via an eigenvalue analysis, to ascertain the presence of streamwise vortices with a preferential spanwise wavelength.

The velocity field $\boldsymbol{v}_2 = [u_2, v_2]$ and the pressure p_2 describing the base flow with transpiration are represented as

$$\boldsymbol{v}_2(x, y) = [U_0(y), 0] + [u_1(x, y), v_1(x, y)], \qquad p_2(x, y) = Px + p_1(x, y), \tag{5.1}$$

where $U_0(y)$ is the mean velocity profile, computed from the reference DNS for the turbulent flow without transpiration, and u_1, v_1 and p_1 are the two-dimensional velocity and pressure modifications due to the presence of the transpiration. The constant P denotes the streamwise pressure gradient of the unmodified flow. Substitution of (5.1) into the Reynolds-averaged Navier–Stokes and continuity equations, introduction of stream function Ψ and elimination of pressure lead to a set of ordinary differential equations for the Fourier coefficients of Ψ, to be solved using a Chebyshev collocation method. The velocity field $\boldsymbol{v}_2$ (or, equivalently, the modification field $\boldsymbol{v}_1$) can be easily computed afterwards. The resulting velocity components are represented in the form

$$u_1(x, y) = \sum_{n=-\infty}^{n=+\infty} U^{(n)}(y) \mathrm{e}^{\mathrm{i}n\alpha_t x}, \qquad v_1(x, y) = \sum_{n=-\infty}^{n=+\infty} V^{(n)}(y) \mathrm{e}^{\mathrm{i}n\alpha_t x}. \tag{5.2}$$

Unsteady, three-dimensional disturbances $\boldsymbol{v}_3$ and p_3 are then superimposed on the two-dimensional solution, in the form

$$\boldsymbol{v} = \boldsymbol{v}_2(x, y) + \boldsymbol{v}_3(x, y, z, t), \qquad p = p_2(x, y) + p_3(x, y, z, t). \tag{5.3}$$

This assumed form of the flow is substituted into the field equations, the mean part is subtracted and the equations are linearized. Our interest is in disturbances in the form of streamwise vortices and thus the solution is assumed in the form

$$[u_3, v_3, p_3] = [\hat{u}_3(x, y), \hat{v}_3(x, y), \hat{p}_3(x, y)] \cos(\beta z)\, \mathrm{e}^{\sigma t}, \tag{5.4a}$$

$$w_3 = \hat{w}_3(x, y) \sin(\beta z)\, \mathrm{e}^{\sigma t}, \tag{5.4b}$$

where β is the spanwise wavenumber of the vortices and σ is their amplification rate. The disturbance field is subject to periodic modulation in the streamwise direction:

$$\hat{q}_3(x, y) = \sum_{n=-\infty}^{n=+\infty} q^{(n)}(y) \mathrm{e}^{\mathrm{i}n\alpha_t x}, \tag{5.5}$$

where $\hat{q}_3$ is real and stands for any flow quantity (i.e. $\hat{u}_3$, $\hat{v}_3$, $\hat{w}_3$, $\hat{p}_3$), $q^{(n)} = q^{(-n)*}$ and a star denotes complex conjugate. Substitution of (5.2) and (5.5) into the equations of motion and some re-arrangements lead to a system of equations for each pair $(u^{(n)}, v^{(n)}), n \geqslant 0$, subject to homogeneous boundary conditions. The differential problem is an eigenvalue problem for the amplification rate σ. Its numerical solution involves truncating the sum in (5.5) after a finite number N of terms, using the collocation method to discretize the retained equations and spectral decomposition of the resulting matrix.

The key assumption in this procedure is the role of turbulent fluctuations. As a first step, fluctuations can be neglected, and the analysis can be carried out as in the laminar case, with the turbulent mean velocity profile $\langle u(y) \rangle$ for the impermeable case taking the role of the parabolic Poiseuille profile as the base flow $U_0(y)$. In this case, documented by Quadrio, Floryan & Luchini (2005), the stability results do not agree with DNS data, and predict the development of large-scale vortical structures in the turbulent flow, with the largest instability taking place for a spanwise wavenumber of $\beta h \approx 2.5$ when the transpiration wavenumber is $\alpha_t = 1.8$ (at intensity $A/U_c = 0.004$).

A better way to account for turbulence fluctuations is modelling Reynolds stresses via a variable eddy viscosity: this approach has been followed by, among others, Reynolds & Tiedermann (1967), Jiménez *et al.* (2001) and Reau & Tumin (2002). If we define

$$M = 1 + \nu_t = -\frac{y(\mathrm{d}U_0/\mathrm{d}y)_{y=-1}}{\mathrm{d}U_0/\mathrm{d}y},$$

where M stands for the viscosity made dimensionless using the molecular viscosity and ν_t denotes the dimensionless eddy viscosity, the outcome of the analysis is different: now the prediction is that vortices do not develop, since disturbances of the form (5.4) decay in time for any combination of β and A. This suggests that low-Reynolds-number effects, together with diffusion due to turbulence, may explain the absence of the large structures, which might however be observed in datasets obtained from higher-Re experiments or simulations.

Limitations in computational resources prevented us from exploring whether the presence of streamwise vortices can be detected at much higher Re. We can however shed some light on the validity of the present approach, by comparing the field $\boldsymbol{v}_1$ as extracted from the DNS database to the same quantity as computed from the

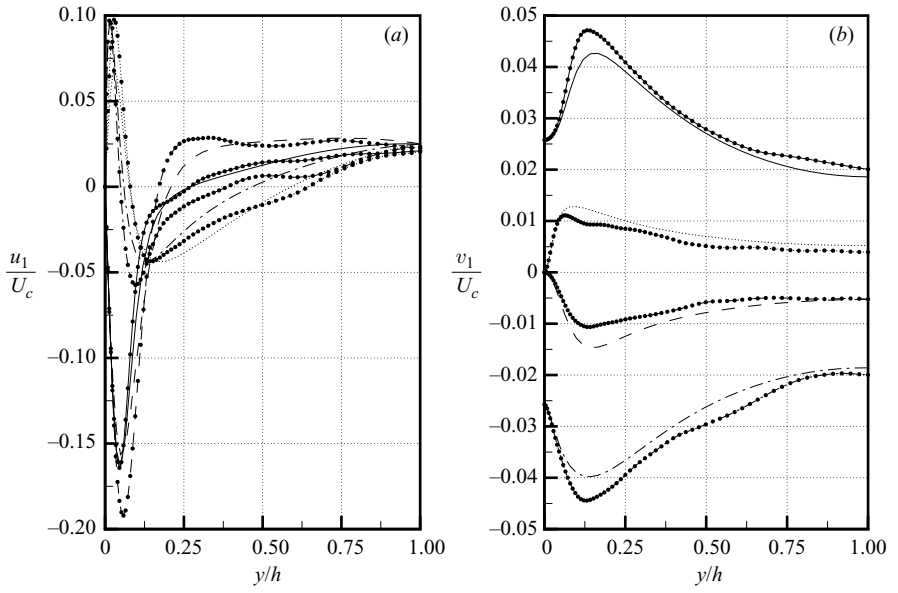

FIGURE 12. Field $\boldsymbol{v_1}$ computed following the method described in § 5.2 with turbulent viscosity (lines) and extracted from the DNS database (symbols), for $Re = 2833$, suction amplitude $A/U_c = 0.0254$ and $\alpha_t h = 2.0$. (*a*) u_1 component. (*b*) v_1 component. Different line types correspond to different positions along the transpiration wave. Continuous: $x/\lambda_t = 0$; dashed: $x/\lambda_t = 0.25$; dash-dotted: $x/\lambda_t = 0.5$; dotted: $x/\lambda_t = 0.75$.

above-mentioned assumptions, with turbulent viscosity turned on. It can be seen in figure 12 that the overall features of the mean flow modifications induced by transpiration are captured quite well by our relatively simple analysis. Some differences can be observed however, particularly in the near-wall region for the u_1 profile and over the suction part. The v_1 profiles are reproduced well, though the DNS shows slightly larger maxima at $x/\lambda_t = 0$ and $x/\lambda_t = 0.5$, and smaller ones at $x/\lambda_t = 0.25$ and $x/\lambda_t = 0.75$. If one considers the sweeping modelling assumptions behind our analysis, the present results provide encouragement that such an analysis would give at least qualitative guidance.

6. Conclusions

The effect of a sinusoidal distribution of transpiration at the walls of a turbulent channel flow has been examined, by carrying out a number of direct numerical simulations and by systematically changing both the intensity A^+ and the wavelength λ_t^+ of the forcing. A significant effect of λ_t^+ has been noticed.

For long wavelengths, there is a dramatic increase in frictional drag the turbulent drag for relatively small values of the transpiration intensity. The increase in frictional drag C_f has been quantified for a wide range of parameters.

When the transpiration wavelength is decreased below a threshold value, given by $\lambda_t^+ \approx 350$, the drag increase disappears, and an opposite effect takes place: a small but definite reduction of the frictional drag. These variations of C_f, which are sometimes small in absolute terms, have been demonstrated to be neither an artifact of numerical inaccuracies, nor a low-Re effect. We have measured a drag reduction of up to 13.0 %

for $A^+ = 4.7$ and $\lambda_t^+ = 226$. The scaling of the threshold wavelength in wall units has been verified by running a few simulations at a higher value of the Reynolds number. Below the threshold value of λ_t^+, which has been linked to a typical length scale of the near-wall turbulence cycle, the transpiration effectively interacts with the near-wall streamwise vortices to shield the wall from the high-friction events connected with them. The physical mechanism for this drag reduction phenomenon is the reduction of turbulent fluctuations, due to the combined action of extracting turbulent fluid through suction and of blowing fluctuationless fluid into the flow. The transpiration wave at the wall produces an additional effect, due to steady streaming, which has been shown to be always in the direction of increasing the drag, at least in the range of parameters considered. (We are aware of laminar-flow examples where the effect of streaming is drag-reducing for some wavenumbers and drag-increasing for others.)

Despite their potential application appeal, large-scale streamwise vortices have not been found in the flow, at least for the present value of the Reynolds number: it can thus be concluded that turbulent diffusion overwhelms the curvature-induced instability mechanism, which is responsible for the appearance of such vortices in the laminar regime. While vortices may exist at higher values of *Re*, at the present *Re* flow perturbations appear to be stable, according to a stability analysis of the mean velocity profile, made in analogy with the laminar case. The two-dimensional base flow induced by transpiration and computed in the stability analysis is found to be in agreement with DNS results, thus corroborating the approach of studying – at least qualitatively – a turbulent flow through a stability analysis of its mean velocity profile, and accounting for the effects of turbulence fluctuations via the turbulent viscosity concept.

This work has been carried out with support of NSERC and SHARCNET of Canada. SHARCNET of Canada provided part of the computing resources, while some simulations have been run on the Opteron system by P. L. at the Università di Salerno. Preliminary results have been communicated by M. Q. at the 49th Annual Meeting of the Canadian Aeronautics and Space Institute, Montréal, April 2003, and at the 5th Euromech Fluid Mechanics Conference, Toulouse, August 2003.

Appendix. Accuracy check

We give here a brief account of the accuracy of the time-averaged value of the friction coefficient, computed according to its definition (3.1), for the simulations at $Re_\tau = 180$.

The discretization parameters listed in § 2.1 match those employed by Kim *et al.* (1987) in their widely quoted DNS of turbulent channel flow at the same value of *Re*. We are thus confident in the accuracy of our results for the impermeable case. In fact we compute for $A = 0$ a value of $C_f = 8.15 \times 10^{-3}$, which differs from the value reported by Kim *et al.* by 0.4 % only.

When transpiration is applied, the physics of the flow changes, as do the spatial gradients of the flow variables. Strong shear layers are present, as noticed for example by Park *et al.* (2001) in their pulsating suction experiments. We have therefore carried out a number of additional simulations, including – but not limited to – spatial-resolution checks, with the aim of assessing the error margins of the results: they are summarized in table 1. We have selected three particular test cases, identified by

	N_y	N_x	N_z	Δy^+_{max}	Δx^+	Δz^+	$10^3 C_f$	ϵ	ϵ_d
case A	129	193	161	7.3	17.9	10.8	12.40	–	–
A1	*257*	193	161	*3.7*	17.9	10.8	12.34	−0.5	1.4
case B	129	193	161	4.6	11.3	6.8	7.85	–	–
B1	*257*	193	129	*2.3*	11.3	6.8	7.86	+0.1	3.3
B2	129	*385*	161	4.6	*5.7*	6.8	7.89	+0.4	13.3
B3	129	193	*321*	4.6	11.3	*3.4*	7.85	+0.0	0.0
B4	129	193	161	4.6	11.3	6.8	7.86	+0.2	6.6
B5	129	193	161	4.6	11.3	6.8	7.89	+0.4	12.0
case C	129	193	161	4.4	10.9	6.6	7.55	–	–
C1	*257*	193	161	*2.2*	10.9	6.6	7.68	+1.7	21.6

TABLE 1. Dependence of the computed value of C_f upon the discretization parameters, for three representative cases at $Re_\tau = 180$, indicated as case A ($\lambda_t^+ = 565$ and $A^+ = 0.7$), case B ($\lambda_t^+ = 226$ and $A^+ = 0.7$), and case C ($\lambda_t^+ = 226$ and $A^+ = 2.82$). Departures from the baseline parameters are indicated in italics. The corresponding friction velocity of each case is used to express the size of the computational grid in wall units, and Δy^+_{max} is the maximum spacing in the wall-normal direction. The percentage errors ϵ and ϵ_d are defined in the text. In run B4 transpiration has been applied to one wall only. In run B5 transpiration has been applied at both walls according to the boundary conditions (A 1).

specific combinations of A and λ_t. They are representative of simulations with small A and large λ_t (case A), small A and small λ_t (case B), large A and small λ_t (case C).

Runs A1, B1–B3 and C1 are resolution checks, where the number of points in one direction is doubled. In run B4 transpiration is applied at one wall only. Run B5 has transpiration applied on both walls, but, unlike the baseline boundary condition given by (2.1), here at a given x position suction at one wall corresponds to suction on the opposite wall too, i.e.

$$v(x, -1, z) = A\cos(\alpha_t x), \qquad v(x, +1, z) = -A\cos(\alpha_t x). \tag{A 1}$$

In table 1 two quantities are computed, defined as

$$\epsilon = 100\,\frac{C_{f,check} - C_{f,t}}{C_{f,t}}, \qquad \epsilon_d = 100\,\left|\frac{C_{f,check} - C_{f,t}}{C_{f,0} - C_{f,t}}\right|.$$

Here $C_{f,0}$ is the friction coefficient computed in the impermeable case, $C_{f,t}$ is the friction coefficient computed with transpiration turned on and with the baseline computational parameters previously described in § 2.1, and $C_{f,check}$ is the friction coefficient computed in the current check; ϵ is an estimate of the percentage error in the evaluation of C_f, while ϵ_d is representative of the percentage error in the change of C_f due to a given distribution of transpiration.

When transpiration causes C_f to increase significantly above the impermeable value (case A), the spatial resolution becomes only just sufficient owing to the overall increase of the friction Reynolds number, but ϵ_d remains small, of the order of 1 %. In the most interesting region where the turbulent friction is reduced, the resolution study indicates that only the streamwise resolution is increasing worth further, with an ϵ_d of the order of 10 % and an absolute error below 1 %. However, when the transpiration intensity is larger (case C), ϵ remains low but the percentage error in the variation in C_f, as indicated by ϵ_d, is not negligible anymore, amounting to approximately 20 %. This motivated us to carry out several simulations (described in connection with

figure 3), and particularly those with transpiration intensity $A^+ \geqslant 2.35$, with doubled resolution in all spatial directions.

REFERENCES

Ahn, J., Sung Jung, I. & Lee, J. 2003 Film cooling from two rows of holes with opposite orientation angles: injectant behavior and adiabatic film cooling effectiveness. *Intl J. Heat Fluid Flow* **24** (1), 91–99.

Antonia, R., Zhu, Y. & Sokolov, M. 1995 Effect of concentrated wall suction on a turbulent boundary layer. *Phys. Fuids* **7**, 2465–2474.

Choi, H., Moin, P. & Kim, J. 1994 Active turbulence control for drag reduction in wall-bounded flows. *J. Fluid Mech.* **262**, 75–110.

Chung, Y., Sung, H. & Krogstad, P.-A. 2002 Modulation of near-wall turbulence structure with wall blowing and suction. *AIAA J.* **40** (8), 1529–1535.

Crighton, D. & Gaster, M. 1976 Stability of slowly diverging jet flow. *J. Fluid Mech.* **77**, 397–413.

Floryan, J. 1997 Stability of wall-bounded shear layers in the presence of simulated distributed roughness. *J. Fluid Mech.* **335**, 29–55.

Floryan, J. 2003 Wall-transpiration-induced instabilities in plane Couette flow. *J. Fluid Mech.* **488**, 151–188.

Gad-el Hak, M. & Bushnell, D. 1991 Separation control: review. *Trans. ASME: J. Fluids Engng* **113** (3), 5–29.

Gong, W., Taylor, P. & Dörnbrack, A. 1996 Turbulent boundary-layer flow over fixed aerodynamically rough two-dimensional sinusoidal waves. *J. Fluid Mech.* **312**, 1–37.

Gschwind, P., Regele, P. & Kottke, V. 1995 Sinusoidal wavy channel with Taylor-Görtler vortices. *Expl Therm. Fluid Sci.* **11**, 270–275.

Günther, A. & Rudolph von Rohr, P. 2003 Large-scale structures in a developed flow over a wavy wall. *J. Fluid Mech.* **478**, 257–285.

Iwamoto, K., Fukagata, K., Kasagi, N. & Suzuki, Y. 2005 Friction drag reduction achievable with near-wall manipulation at high Reynolds numbers. *Phys. Fluids* **17**, 011702.

Jeong, J., Hussain, F., Schoppa, W. & Kim, J. 1997 Coherent structures near the wall in a turbulent channel flow. *J. Fluid Mech.* **332**, 185–214.

Jiménez, J. & Moin, P. 1991 The minimal flow unit in near-wall turbulence. *J. Fluid Mech.* **225**, 213–240.

Jiménez, J., Uhlmann, M., Pinelli, A. & Kawahara, G. 2001 Turbulent shear flow over active and passive porous surfaces. *J. Fluid Mech.* **442**, 89–117.

Kim, J., Moin, P. & Moser, R. 1987 Turbulence statistics in fully developed channel flow at low Reynolds number. *J. Fluid Mech.* **177**, 133–166.

Leibovich, S. 1983 The form and dynamics of Langmuir circulation. *Annu. Rev. Fluid Mech.* **15**, 391–427.

Luchini, P. & Quadrio, M. 2006 A low-cost parallel implementation of direct numerical simulation of wall turbulence. *J. Comput. Phys.* **211** (2), 551–571.

Park, J. & Choi, H. 1999 Effects of uniform blowing or suction from a spanwise slot on a turbulent boundary layer flow. *Phys. Fluids* **11** (10), 3095–3105.

Park, S.-H., Lee, I. & Sung, H. 2001 Effect of local forcing on a turbulent boundary layer. *Exps. Fluids* **31**, 384–393.

Quadrio, M., Floryan, J. & Luchini, P. 2005 Modification of Turbulent Flow using Distributed Transpiration. *Can. Aeron. Space J.* **51** (2), 61–69.

Quadrio, M. & Luchini, P. 2003 Integral time-space scales in turbulent wall flows. *Phys. Fluids* **15** (8), 2219–2227.

Rayleigh, Lord 1883 On the circulation of air observed in Kundt's tubes and some allied acoustical problems. *Phil. Trans. R. Soc. Lond.* A **175**, 1–21.

Reau, N. & Tumin, A. 2002 On harmonic perturbations in a turbulent mixing layer. *Eur. J. Mech.* B/*Fluids* **21**, 143–155.

Reynolds, W. & Tiedermann, W. 1967 Stability of turbulent channel flow, with application to Malkus' theory. *J. Fluid Mech.* **27**, 253–272.

Riley, N. 2001 Steady streaming. *Annu. Rev. Fluid Mech.* **33**, 43–65.

Schoppa, W. & Hussain, F. 1998 A large-scale control strategy for drag reduction in turbulent boundary layers. *Phys. Fluids* **10** (5), 1049–1051.

Schoppa, W. & Hussain, F. 2002 Coherent structure generation in near-wall turbulence. *J. Fluid Mech.* **453**, 57–108.

Sumitani, Y. & Kasagi, N. 1995 Direct numerical simulation of turbulent transport with uniform wall injection and suction. *AIAA J.* **33** (7), 1220–1228.

Tardu, S. 2001 Active control of near-wall turbulence by local oscillating blowing. *J. Fluid Mech.* **439**, 217–253.